Langmuir−Blodgett Thin Films of Fe$_{20}$Pt$_{80}$ Nanoparticles for the Electrocatalytic Oxidation of Formic Acid

Wei Chen,[†] Jaemin Kim,[‡] Li-Ping Xu,[†] Shouheng Sun,*,[‡] and Shaowei Chen*,[†]

Department of Chemistry and Biochemistry, University of California, Santa Cruz, California 95064, and Department of Chemistry, Brown University, Providence, Rhode Island 02912

The electro-oxidation of formic acid catalyzed by Fe$_{20}$Pt$_{80}$ nanoparticles was studied by cyclic voltammetry (CV) and electrochemical impedance spectroscopy (EIS) where the particles were deposited onto a gold electrode surface by the Langmuir−Blodgett (LB) technique at varied film thickness/coverage. It was found that the particle assembly thickness strongly affected the electrocatalytic activity for HCOOH oxidation. For a single monolayer and two layers of FePt particles, extensive CO adsorption (poisoning) was observed in CV measurements, whereas with a four-layer assembly of the FePt particles, the tolerance to CO poisoning improved drastically. Furthermore, from the current density for formic acid oxidation, the electrodes functionalized with LB layers of nanoparticles exhibited higher activities than those with dropcast films of similar thickness, suggesting the importance of the ordering of the particle layers in the electrocatalytic performance. The reaction kinetics in the HCOOH oxidation on the three kinds of particle film-modified electrodes was then examined by EIS measurements. It was found that except within the potential range for CO oxidation, the impedance spectra behaved normally with the responses shown in the first quadrant for all three nanoparticle assemblies under study, indicative of only resistive and capacitive components in the electrochemical cell. In contrast, at potentials of CO electro-oxidation, the impedance spectra were found to migrate from the first quadrant to the second quadrant and then back to the first quadrant with increasing electrode potential, which suggests that the reaction kinetics evolve from resistive to pseudoinductive and then to inductive behaviors. The different EIS behaviors are ascribed to the different degree of tolerance to CO poisoning, consistent with the voltammetric results.

1. Introduction

Extensive efforts have been devoted to fuel cell research in the past few decades, as fuel cells are considered as the promising candidates of power sources in portable electronic devices and transportation (electrical) vehicles.[1,2] Yet, despite substantial improvements of fuel cell performance in recent years, some challenging obstacles remain.[2−5] Of these, optimization of the electrocatalysts represents a critical step. Noble metals (mainly Pt) have often been employed as the catalysts in fuel cells.[6] Recent studies have shown that Pt-based alloy catalysts[7−15] exhibit greater catalytic activities for the electro-oxidation of small organic fuels such as methanol and formic acid due to the so-called bifunctional mechanism[16−18] or electronic (ligand) effect.[7,19] In order to further reduce the costs of catalysts, either less expensive non-noble metal catalysts have to be used or the loading of the noble metals on the electrode surface has to be reduced, and at the same time, the catalytic performance and utilization efficiency of electrocatalysts remain uncompromised. To this end, it is essential and important to have a mechanistic understanding of the electron-transfer dynamics involved, by carrying out a systematic study with variation of the catalyst structures and assemblies.

For Pt and Pt-based alloy nanostructured catalysts,[20−22] the metal particles were typically studied by dropcasting the colloidal solution onto an electrode surface forming a thick film. However, by using this method, it is very difficult to control the thickness and ordering of the films, as such dropcast films usually are not uniform with extensive structural defects. Since it has been well-known that the surface layers of the particle films play a critical role in the electro-oxidation of formic acid and other fuels,[3,23,24] it is of fundamental and technological significance to examine the effects of particle loading and ordering on the catalytic activities. This can be readily achieved by the Langmuir−Blodgett (LB) technique.

Using formic acid as a model fuel, we have carried out an earlier study with a dropcast thick film of Fe$_{20}$Pt$_{80}$ nanoparticles (average diameter ∼3 nm) and found that the particles exhibited very good electrocatalytic activities for formic acid electro-oxidation,[25] as compared to Pt and other metal alloys. This was motivated, in part, by the fact that aqueous solutions of formic acid have been found to be an attractive potential fuel because of the ease of their handling, transportation, and storage in comparison to hydrogen.[26] In this paper, we carried out further studies to examine the effect of the FePt particle film thickness on the electrocatalytic activities in the oxidation of formic acid. The particle films, from a single monolayer to multilayers, were prepared by the LB technique. The voltammetric and electrochemical impedance measurements showed that the catalytic behaviors of FePt particles were strongly dependent on the assembly thickness, suggestive of a minimal and optimal loading of the nanoparticle catalysts for the fuel cell reactions.

2. Experimental Section

2.1. Chemicals. Perchloric acid (HClO$_4$, Fisher, 99.999%) and formic acid (HCOOH, ACROS, 99%) were used as received. Water was supplied by a Barnstead Nanopure water

* To whom all correspondence should be addressed. E-mail: schen@chemistry.ucsc.edu.
† University of California, Santa Cruz.
‡ Brown University.

system (18.3 MΩ·cm). All solutions were deaerated by bubbling ultrahigh-purity N$_2$ for 20 min and protected with a nitrogen atmosphere during the entire experimental procedure.

2.2. FePt Nanoparticles. The FePt nanoparticles were synthesized according to the procedure described previously,[25] but the composition of the particles was controlled at Fe$_{20}$Pt$_{80}$ to ensure particle stability in strong acid media. Briefly, under a gentle flow of N$_2$, Pt(acetylacetonate)$_2$ (0.5 mmol), 1,2-hexadecanediol (1.5 mmol), and dioctylether or benzyl ether (20 mL) were mixed at room temperature and heated to 100 °C. Oleic acid (0.5 mmol), oleyl amine (0.5 mmol), and Fe(CO)$_5$ (1.0 mmol) were added, and the mixture was heated to reflux (297 °C) for 30 min. (Note: N$_2$ was kept flowing through the reaction system to ensure the Pt-rich Fe$_{20}$Pt$_{80}$ nanoparticles were formed. This was different from the previous synthesis in which the reaction was run under a blanket of N$_2$.) The heat source was removed, and the reaction mixture was cooled down to room temperature. At this point, the reaction system was opened to the ambient environment. The black product was precipitated by adding ethanol (40 mL) and separated by centrifugation. The supernatant was discarded, and the black precipitate was dispersed in hexane (25 mL) in the presence of oleic acid (0.05 mL) and oleylamine (0.05 mL). Then, ethanol (20 mL) was added to the dispersion and the suspension was centrifuged again. The precipitation was redispersed by hexane. From transmission electron microscopic (TEM) measurements, the particle core size was estimated to be 3.98 ± 0.73 nm (a representative TEM micrograph was included in the Supporting Information).

2.3. Preparation of Particle Langmuir−Blodgett Thin Films. The experimental setup has been described in detail previously.[27−29] In a typical experiment, 100 μL of a FePt particle solution (1 mg/mL in CH$_2$Cl$_2$) was spread dropwise by using a Hamilton microliter syringe onto the water surface of a Langmuir−Blodgett trough (NIMA 611D). At least 20 min was allowed for solvent evaporation prior to the first compression and between compression cycles. Compression speed was set at 10 cm^2/min. Prior to particle deposition, a gold film electrode was first treated in an ultraviolet ozone (UVO) chamber (Jelight Company, Inc., model 42) for about 15 min and then coated with a self-assembled monolayer of *n*-butanethiol in order to render the electrode surface hydrophobic. The FePt particles were then transferred onto the gold film electrode surface by the LB technique at a dipping speed of 1 mm/min at controlled surface pressures. Three particle thin films were prepared at the same surface pressure, consisting of one, two, and four monolayers of particles, which were hence referred to as the LB1, LB2, and LB4 electrodes, respectively.

2.4. Atomic Force Microscopy (AFM). The morphology of the LB films was studied by tapping-mode AFM. The AFM images were acquired with a PicoLE SPM instrument (Molecular Imaging Inc.). The scan speed was 1.8 lines/s. All the AFM images were flattened with Molecular Imaging software. For the measurements of the particle layer thickness, the AFM images were first divided into a 20 × 20 matrix and line analyses were carried out of 20 evenly spaced sections in both the vertical and horizontal directions, from which the height information at each crossing point was obtained. The average thickness (and the standard deviation) of the particle films was then estimated.

2.5. Electrochemistry. Voltammetric measurements were carried out with a CHI 440 electrochemical workstation. The FePt particles-coated Au film electrodes were used as the working electrode. Prior to any electrochemical measurements, the electrode was subject to UVO treatment to remove the
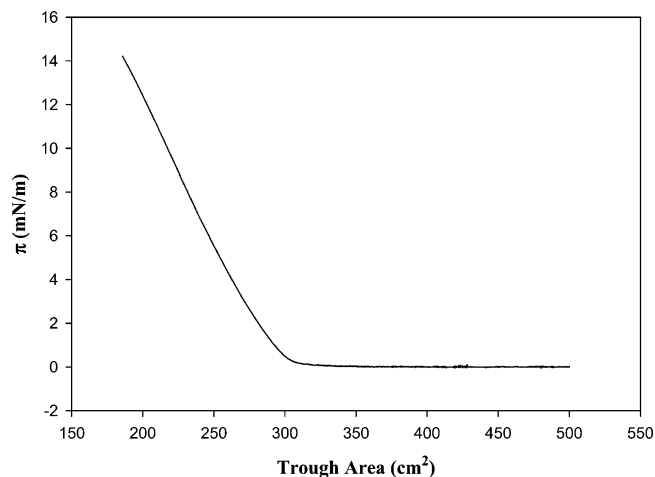

Figure 1. Langmuir isotherm of a Fe$_{20}$Pt$_{80}$ particle monolayer at the air/water interface: particle concentration, 1 mg/mL in CH$_2$Cl$_2$; amount spread, 100 μL; compression speed, 10 cm^2/min.

organic coating around the FePt nanoparticles. A Ag/AgCl wire and a Pt coil were used as the reference and counter electrodes, respectively. All electrode potentials in the present study were referred to this Ag/AgCl quasi-reference. Electrochemical impedance spectroscopy (EIS) measurements were carried out using an EG&G PARC potentiostat/galvanostat (model 283) and frequency response detector (model 1025). The impedance spectra were recorded between 100 kHz and 10 mHz with the amplitude (rms value) of the ac signal 10 mV.

3. Results and Discussion

3.1. Langmuir−Blodgett Thin Films of FePt Nanoparticles. Figure 1 shows the Langmuir isotherm of a FePt particle monolayer at the air|water interface, which is very similar to those observed with other metal and semiconductor nanoparticles,[27−29] with a takeoff area of 290 cm^2. The particles were then transferred onto the electrode surface by the LB technique at the surface pressure of 13.5 mN/m. From the isotherm, the corresponding particle density on the water surface can be estimated to be 0.52 μg/cm^2. Thus, for an ideal deposition, the particle surface density on the electrode surface should be 0.52 (LB1), 1.04 (LB2), and 2.08 μg/cm^2 (LB4), respectively.

Tapping-mode AFM imaging was then carried out to examine the surface morphology and coverage of the deposited particle thin films. Figure 2 shows the corresponding topographical images and line scan profiles of the three LB thin films of nanoparticles. It can be seen that the resulting particle assemblies are all very closely packed, signifying very efficient transfer of the particle layers from the air|water interface onto the electrode surface. Yet, line scans across the AFM images reveal that the surface roughness of the particle LB thin films increases with increasing thickness of the particle assemblies. For instance, the average thickness of the particle layers increases from ca. 6.5 ± 1.5 nm (roughness ratio 23%) in the LB1 sample (panel a) to about 12 ± 2.3 nm (19%) and 20 ± 7.5 nm (38%) in the LB2 (panel b) and LB4 (panel c) samples, respectively. This deviates slightly from the expected 1:2:4 for an ideal deposition. There are at least two plausible explanations to these observations. The first was possibly due to the less efficient transfer of particles for a thicker film, as the AFM image (Figure 2c) shows some clustering of the particles. Measurements of the height of the bright features indicate that they are not of isolated particles but rather a cluster of particles. Additionally, in solid state, it is well-known that intercalation of the surface protecting ligands
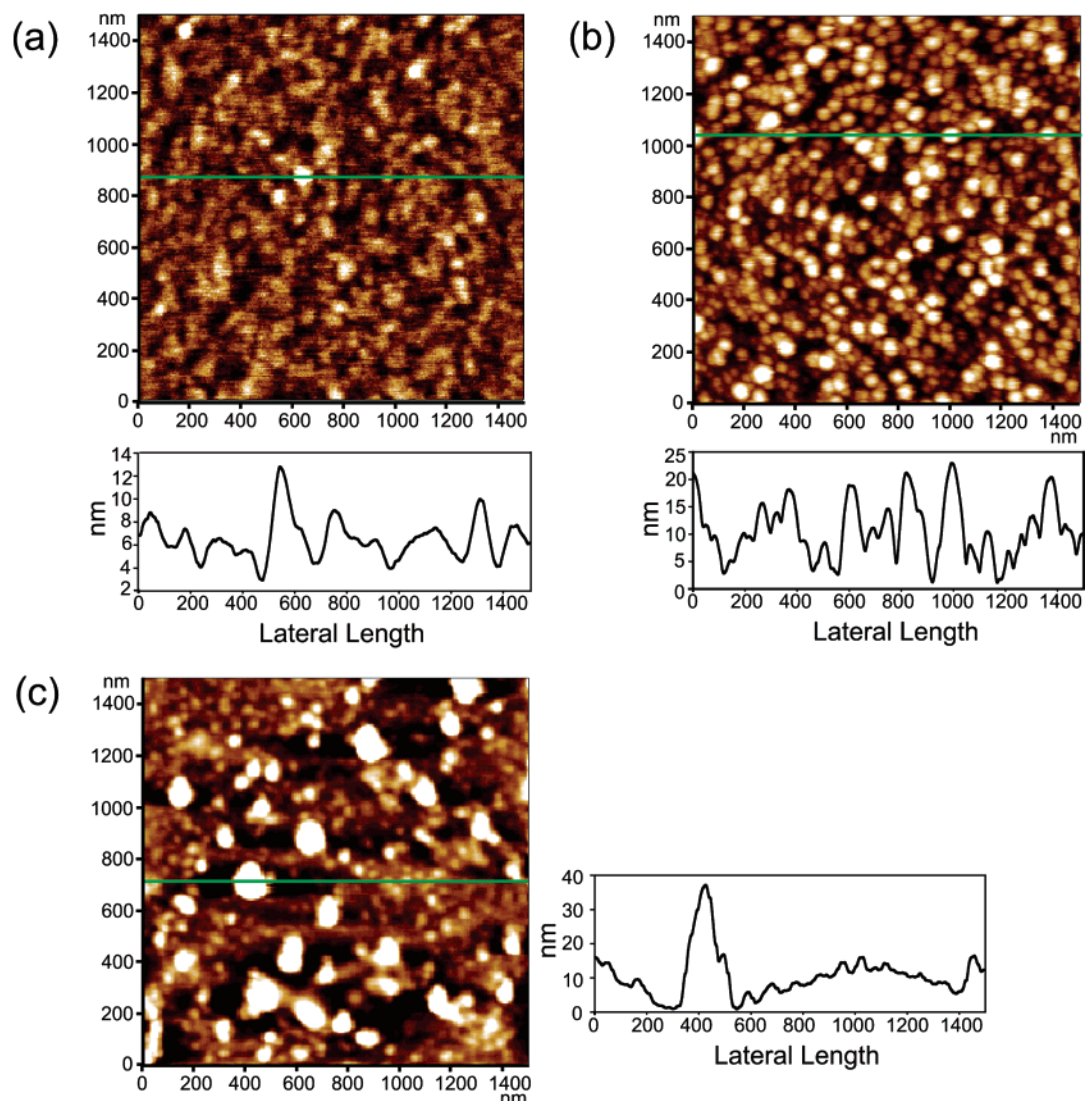
Figure 2. Tapping-mode AFM topographical images and representative line scan profiles of the $Fe_{20}Pt_{80}$ nanoparticle LB films: (a) LB1, (b) LB2, (c) LB4. Scan size is 1500 nm × 1500 nm, and scan rate is 1.8 lines/s.

of organically capped nanoparticles occurs.[30] Thus, when a second layer of particles is deposited onto the electrode surface, it is likely that ligand intercalation will also occur between the layers of particles. Yet the intercalation is probably not uniform across the entire layer, leading to enhanced roughness of the particle films. The resulting surface roughness will propagate with the deposition of more layers of particles. However, it should be noted that the surface roughness observed with the LB films here is significantly lower than that of nanoparticle films prepared by the dropcast method which exhibit extensive clustering of nanoparticles (roughness ratio >30%, Supporting Information).

Also, it should be noted that the thickness measured by tapping-mode AFM in the LB1 particle film reflects the physical diameter of the nanoparticles, which consists of the metal core plus two protecting ligands. Considering the average particle core size of 3.98 nm (from TEM measurements, Supporting Information Figure S1) and the fully extended chain length of an oleic acid or oleylamine around 2.0 nm (from Hyperchem), the results are reasonable.

3.2. Electrochemistry of PtFe Functionalized Electrodes. In the previous studies of FePt alloy electrodes, it has been found that during the electrochemical scans, there will be a Pt skin formed on the electrode surface due to the dissolution of Fe on

the surface of FePt alloys.[31,32] Thus, the resulting steady-state cyclic voltammograms usually behave similarly to those of pure Pt. Figure 3 shows the stead-state cyclic voltammograms of the three FePt particle films (LB1, LB2, and LB4) in 0.1 M $HClO_4$, which are all similar to those of other Pt-based alloys.[25] (Note that the voltammetric features from the Au film substrate were markedly suppressed, signifying efficient deposition of the particle layers on the electrode surface. Additional cyclic voltammograms are included in Supporting Information.) At low potentials, there are a pair of broad current peaks between −0.50 and −0.27 V which are attributed to the adsorption−desorption of hydrogen on the particle (Pt) surface (at more negative potentials, extensive hydrogen evolution occurred). This feature becomes better-defined with thicker particle films. In addition, in the negative potential scan, there is a reduction current peak around +0.11 V which can be ascribed to the reduction of platinum oxides formed at more positive potentials during the positive potential scan. It should be noted that the current of hydrogen adsorption−desorption and the reduction current of platinum oxides increase with increasing particle layer thickness. On the basis of the charge integration within the hydrogen adsorption−desorption potential region, the actual surface (Pt) area of the three particle films can be evaluated, which is 0.36 (LB1), 0.52 (LB2), and 1.19 cm^2 (LB4), respectively. Note that
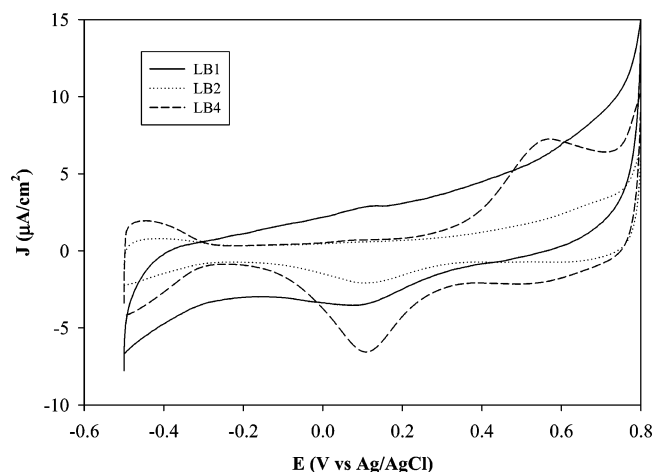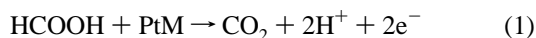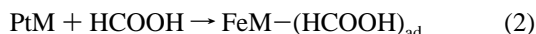
LB Thin Films of Fe$_{20}$Pt$_{80}$ Nanoparticles

J. Phys. Chem. C, Vol. 111, No. 36, 2007 **13455**

Figure 3. Cyclic voltammograms of the Au film electrode coated with the three different particle LB layers in 0.1 M HClO$_4$: potential scan rate, 0.1 V/s. The currents are all normalized to the Au film surface area (0.66 cm^2).

Figure 4. Cyclic voltammograms of the Au electrode coated with the LB1, LB2, and LB4 Fe$_{20}$Pt$_{80}$ particle thin films in 0.1 M HCOOH + 0.1 M HClO$_4$: potential scan rate, 0.02 V/s; gold film surface area, 0.66 cm^2. The currents are all normalized to the respective Pt surface areas that are evaluated from Figure 3.

the ratio of these areas, 1:1.4:3.3, is close to the thickness ratio calculated from the AFM measurements (Figure 2), 1:1.9:3.1, which suggests that the active surface area does increase almost proportionally with the surface density of nanoparticles, and thus the majority of the particles are electrochemically accessible even with thicker particle layers. In contrast, for nanoparticle dropcast films of comparable thickness, the effective surface area is much smaller, primarily because of the clustering of the nanoparticles that limits the accessibility of the catalyst surface (Supporting Information).

3.3. Formic Acid Oxidation. In the last decades, the mechanism of formic acid electro-oxidation on Pt and Pt-based alloys has been investigated extensively, and it is generally accepted that formic acid is oxidized to CO$_2$ via the so-called dual-pathway mechanism.[33−35] For Pt-based alloys (PtM), formic acid can be oxidized to CO$_2$ by the direct pathway,

$$HCOOH + PtM \rightarrow CO_2 + 2H^+ + 2e^- \qquad (1)$$

Alternatively, in the indirect pathway, HCOOH first reacts to form poisonous CO intermediate, which is then oxidized to CO$_2$,

$$PtM + HCOOH \rightarrow FeM-(HCOOH)_{ad} \qquad (2)$$

$$PtM-(HCOOH)_{ad} \rightarrow PtM-(CO)_{ad} + H_2O \qquad (3)$$

$$PtM + H_2O \rightarrow PtM-(OH)_{ad} + H^+ + e^- \qquad (4)$$

$$PtM-(CO)_{ad} + PtM-(OH)_{ad} \rightarrow CO_2 + H^+ + e^- \qquad (5)$$

In both cases, the overall reaction is

$$HCOOH \rightarrow CO_2 + 2H^+ + 2e^- \qquad (6)$$

It has been found in our previous study[25] that from the onset potential and current densities, dropcast films of Fe$_{20}$Pt$_{80}$ nanoparticles exhibit very good electrocatalytic activities for HCOOH oxidation as compared to Pt and other metal alloys.[33−35] However, from the voltammetric currents of HCOOH oxidation in the positive and negative scans, the particles are found to be heavily poisoned by adsorbed CO species. Figure 4 depicts the steady-state cyclic voltammograms of the gold film electrode loaded with the three FePt particle films in 0.1 M HCOOH and 0.1 M HClO$_4$. It can be seen that the voltammetric features
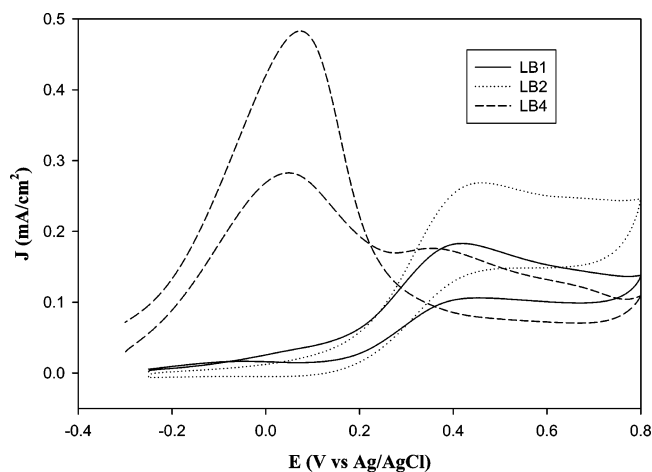
exhibit a rather substantial variation with the nanoparticle layer thickness. For the LB1 and LB2 thin films, in the positive potential scan, an oxidation current peak can be observed at about +0.42 and +0.46 V, respectively; and in the negative potential scan, an oxidation peak at almost the same potential is observed. However, the cathodic current density is somewhat smaller than the anodic one. This can be attributed to the effect of the formation of CO poisoning intermediate and its adsorption onto the catalyst surface. In the positive potential scan, when the electrode potential is scanned from −0.3 to +0.4 V, the oxidation of particle-bound CO starts to occur, leading to the recovery of the catalyst active sites on which direct electro-oxidation of formic acid can now take place. That is, the anodic currents measured reflect the combined contributions from the electro-oxidation of both CO intermediates and formic acid, whereas in the negative potential scan, the currents mostly arise from the formic acid oxidation alone.

For the LB4 nanoparticle film, the cyclic voltammetry (CV) responses are drastically different. There are two current peaks in the positive potential scan, one with a higher intensity at about +0.07 V and the other with a weaker current density at +0.36 V; and in the negative potential scan, a very large oxidation current peak can be seen at about +0.07 V. Similar voltammetric features have also been observed in the studies of electro-oxidation of HCOOH on Pt and other Pt-based alloy electrodes.[36,37] It is well-known that during the electro-oxidation of methanol, formic acid, and other small organic molecules, the so-called dual-pathway mechanism exists which involves a reactive intermediate (direct path, eq 1) and adsorbed CO as a poisoning intermediate species (indirect path, eqs 2−5). For formic acid oxidation at the LB4 electrode, the two oxidation peaks observed in the positive potential scan can be accounted for by the effects of CO poisonous species, because the CO adsorption occurs within the hydrogen region and the double-layer region, and consequently parts of the FePt particle surface become inactive for formic acid oxidation (the poisoning effect). Here the major peak at +0.07 V can be attributable to the direct oxidation of formic acid into CO$_2$ at active surface sites which have not been poisoned by CO adsorption (eq 1), whereas the minor peak at +0.36 V is from the oxidation of the adsorbed CO and of formic acid as a consequence of the release of surface-active sites by CO stripping (eqs 2−5).
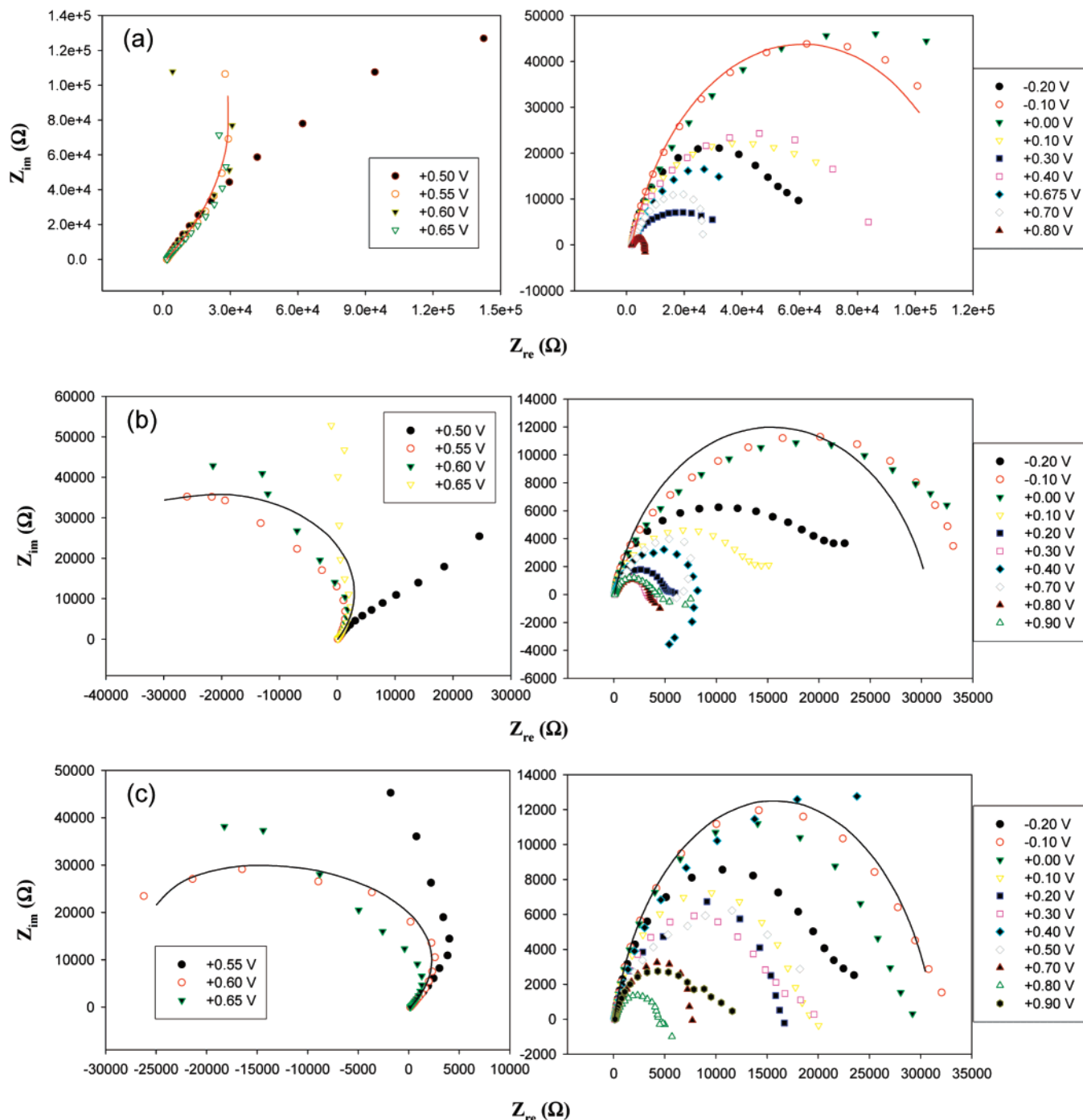
Figure 5. Complex-plane electrochemical impedance plots (Nyquist plots) of the Au film electrode functionalized with varied LB layers of the $Fe_{20}Pt_{80}$ nanoparticles: (a) LB1, (b) LB2, and (c) LB4 in 0.1 M HCOOH + 0.1 M HClO$_4$ at different electrode potentials which are shown in the figure legends. Solid lines are representative curve fits by the equivalent circuits shown in Figure 8.

With further increase in electrode potentials, the adsorbed CO will be removed. So the enhanced peak current of formic acid oxidation observed in the reverse negative potential scan, as compared with that in the positive scan, can be explained by the recovery of all the surface-active sites.

However, at the LB1 and LB2 thin film electrodes, there is only one oxidation peak in both positive and negative potential scans at substantially more positive potentials. The discrepancy in the voltammetric responses may be explained by the different CO poisoning on these particle thin film electrodes. For the LB1 and LB2 thin films, the particle surfaces appear to be easily poisoned by CO adsorption. So the direct oxidation of formic acid is blocked before CO is removed by electro-oxidation. In

contrast, at the LB4 electrode, not all surface-active sites are poisoned by CO adsorption; thus, the direct oxidation of formic acid can occur, which is reflected by the anodic peak at a less positive potential (+0.07 V). Moreover, for LB1 and LB2, the peak current in the negative potential scan is smaller than that in the positive potential scan, which is different from that for LB4. Similar phenomena have also been observed in the electrocatalytic oxidation of HCOOH and CH$_3$OH.[38−44] For instance, in the study of formic acid oxidation on a Au(111) surface modified with Pd layers, it was found that the peak current in the negative potential scan was smaller than that in the positive potential scan when only a single monolayer of Pd was deposited on the Au(111) surface.[12] Such voltammetric

LB Thin Films of Fe$_{20}$Pt$_{80}$ Nanoparticles

J. Phys. Chem. C, Vol. 111, No. 36, 2007 **13457**

features were ascribed to the rapid CO accumulation on the electrode surface.[44] In the present study, the difference of the voltammetric behaviors may also be accounted for by CO accumulation on the LB1 and LB2 electrode surface leading to heavier poisoning than at the LB4 surface.

We would like to point out that in our previous studies[25] with a dropcast thick film of FePt nanoparticles (about nine layers), the catalyst layers were much more extensively poisoned by adsorbed CO species. From the current ratio of the anodic and cathodic peaks for formic acid direct oxidation, the fraction of the catalyst surface that was blocked by CO adsorption was estimated to be 90%.[25] In the present study with the LB4 electrode, this fraction was found to decrease to 42% (Figure 4). These results indicate that there exists a minimal (and optimal) loading of the electrocatalysts in the electro-oxidation of formic acid with improved resistance to CO poisoning.

In addition, on the basis of the current density of the formic acid oxidation, the electrodes functionalized with particle LB layers (Figure 4) exhibited much higher catalytic activities than those with dropcast films of the same particles of similar layer thickness (Figure S4, Supporting Information), suggesting the important role of particle arrangements in the determination of their electrocatalytic performance.

3.4. Electrochemical Impedance Studies. Electrochemical impedance spectroscopy has been a powerful and sensitive technique to study electrochemical kinetics, for instance, in the investigations of the electro-oxidation process of small organic molecules in fuel cells.[45−48] From the voltammetric studies presented above, it can be seen that the loading of the FePt nanoparticle catalysts strongly affects the electrochemical reaction dynamics of formic acid oxidation, which were further examined by EIS measurements, as presented below.

Figure 5 shows the Nyquist complex-plane impedance spectra of the electrodes with one, two, and four FePt particle layers in 0.1 M HCOOH and 0.1 M HClO$_4$ at varied electrode potentials from −0.3 to +0.9 V (shown as figure legends). It can be seen from Figure 5a that for the LB1 electrode, at negative potentials (−0.2 to 0.0 V) the diameter of the arcs (indicating the presence of resistive and capacitive components) exhibits a small increase with increasing electrode potential. This may be ascribed to the formation of intermediate poisoning (CO) species in the potential range that impedes the electro-oxidation of formic acid. With further increase of the electrode potential from 0.0 to +0.3 V, the diameter of the arc in Figure 5a decreases because the electro-oxidation and hence removal of the adsorbed poisoning species starts to occur. At more positive electrode potentials (+0.55 to +0.65 V), the arc bends from the positive to negative direction of the *x*-axis (left panel of Figure 5a), signifying the electro-oxidation process of adsorbed CO, and hence the electrode exhibits pseudoinductive behaviors. Further increase of electrode potentials saw the impedance spectra return to the normal behaviors; and the arc diameter decreases with electrode potentials, indicative of enhanced electron-transfer kinetics.

Figure 5b depicts the impedance spectra with the LB2 particle film in the same electrolyte solution. We can see that at the potentials less than +0.5 V, the impedances plots show almost the same features as those of the LB1 particle film. However, at the potentials between +0.55 and +0.65 V, the impedance starts to appear in the second quadrant instead of the conventional first one. Such negative faradaic impedance is often observed in systems containing adsorbed intermediates and metal surface corrosion,[47−49] which suggests the presence of an inductive component. For the present system, the presence of negative faradic impedance (the inductive component) may be
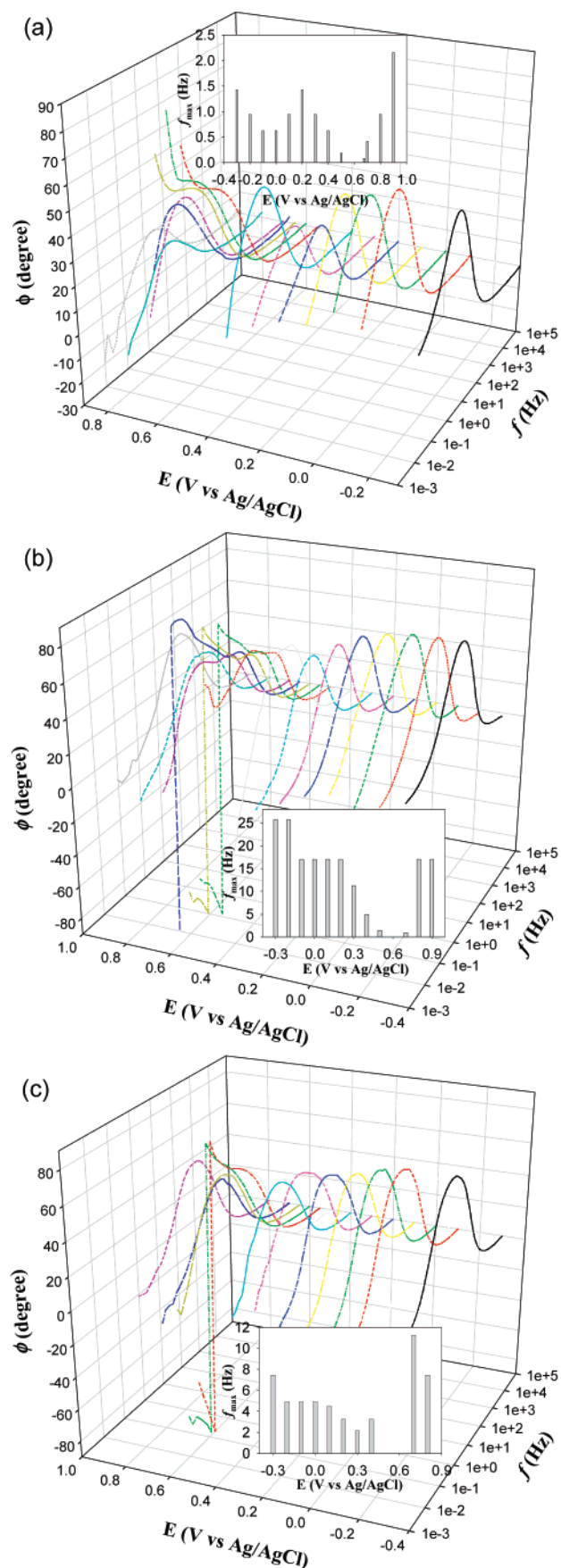

Figure 6. Three-dimensional Bode plots of the electrochemical impedance phase angle of the Au film electrode functionalized with different LB layers of the Fe$_{20}$Pt$_{80}$ nanoparticles: (a) LB1, (b) LB2, and (c) LB4 in 0.1 M HCOOH + 0.1 M HClO$_4$ at various electrode potentials. Insets show the corresponding peak frequency at varied electrode potentials.
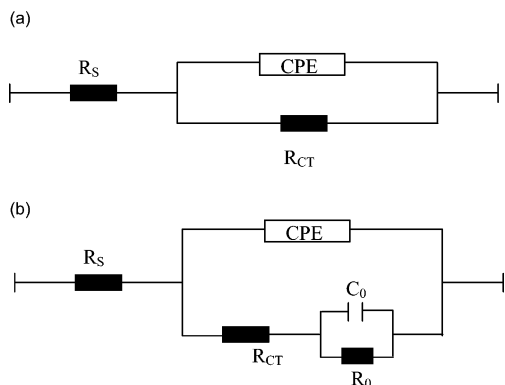
(a)

(b)

Figure 7. Equivalent circuits for the electro-oxidation of formic acid on the $Fe_{20}Pt_{80}$ LB thin film electrodes: (a) for normal impedance and (b) for negative impedance shown in Figures 5 and 6.
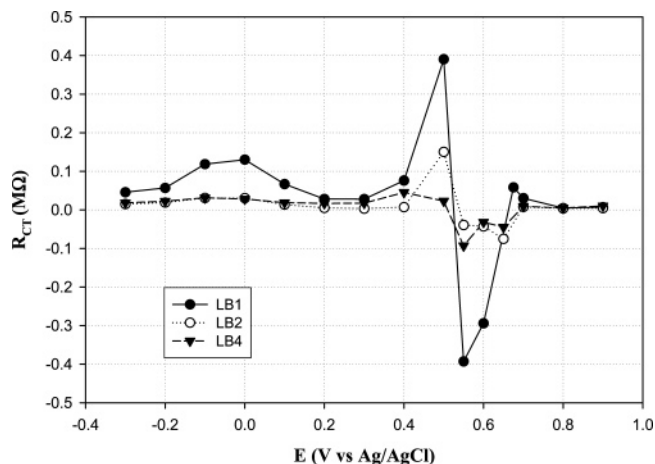

Figure 8. Dependence of charge-transfer resistance (RCT) on electrode potentials for the electro-oxidation of formic acid at the three particle thin film electrodes.

due to the oxidative removal of the adsorbed CO intermediate because of the formation of chemisorbed hydroxyl species in the potential range. From the voltammetric response of HCOOH oxidation at the LB2 nanoparticle film (Figure 4), it can be seen that within the potential range of +0.55 to +0.65 V, the adsorbed intermediates (CO) become oxidized. The impedance results agree well with the above voltammetric studies. When the potential is more positive than +0.65 V, the impedance plots return to the normal Nyquist spectra in the first quadrant. In accord with the impedance change, the voltammetric response of the LB2 film in Figure 4 shows that at potentials greater than +0.65 V, the adsorbed intermediate should be removed by electro-oxidation and platinum oxides begin to be formed.

For the LB4 nanoparticle film (Figure 5c), in comparison with the impedance spectra of the LB2 electrode, the diminishment of the diameter of the negative arcs from +0.55 to +0.65 V implies that more inductive component and less CO poisoning are present in the electrochemical system, consistent with the voltammetric results presented earlier (Figure 4). It should be noted that the impedance results observed here (Figure 5c) are very similar to those with dropcast thick films of the same particles[25] except for a small difference of the potentials at which the negative impedance starts to appear.

Figure 6 depicts the corresponding Bode plots of the LB1, LB2, and LB4 thin film electrodes. It can be seen that there is a maximum phase angle at a characteristic frequency (f_{max}) in all the three Bode plots (insets in each Bode plot display the variation of this characteristic frequency with electrode potentials). This characteristic frequency usually represents the time constant of the electrochemical reaction.[46,47] From Figure 6, it can be seen that f_{max} displays no drastic change with electrode potentials, similar to that observed earlier with FePt dropcast multilayers.[25] Of note is that for the LB2 and LB4 films, an abrupt change of sign of the phase angle was observed in the range of from +0.55 to +0.65 V, which was attributed to the oxidation of adsorbed CO and the resulting inductive behaviors of the electrodes (i.e., negative faradaic impedance).

On the basis of the above voltammetric and impedance measurements, the equivalent circuit for multilayer films of FePt particle[25] was then used to model the impedance responses of the LB1, LB2, and LB4 thin films in this study (Figure 7). Figure 7a depicts the equivalent circuit for the electrodes that exhibit normal impedance behaviors, where R_S represents the solution resistance, CPE (constant-phase element) and R_{CT} are the double-layer capacitance and charge-transfer resistance, respectively. For negative impedance, the equivalent circuit is shown in Figure 7b, where C_0 and R_0 represent the capacitance and resistance of the electro-oxidation of adsorbed CO intermediates.

Several representative fits (solid lines) at both negative and positive electrode potentials were shown in each of the Nyquist plots in Figure 5. From the fitting, it can be seen that the charge-transfer resistance (R_{CT}) exhibits a very substantial dependence on the electrode potential for the three LB films (Figure 8), and more importantly, the charge-transfer resistance for formic acid electro-oxidation decreases with increasing thickness of the particle layers, LB1 > LB2 ≈ LB4, again in good agreement with the above voltammetric and impedance measurements. Furthermore, the charge-transfer resistances observed here with the particle LB thin films were all drastically smaller than those observed earlier[25] with a dropcast thick film of the same particles (approximately nine layers), which implies that the ordering of the electrocatalysts on the electrode surface might also play an important role in the optimization of the overall catalytic activities, as suggested in the aforementioned voltammetric studies.

4. Conclusion

In this report, $Fe_{20}Pt_{80}$ particle layers of varied thickness were prepared by the LB technique and the corresponding electro-catalytic activities for the oxidation of formic acid in an acidic electrolyte were examined by voltammetry and EIS. The voltammetric responses exhibited rather drastic variation with the particle layer thickness. For thinner particle films (LB1 and LB2), the direct electro-oxidation of formic acid was impeded significantly by the adsorption of poisonous CO species (heavy CO poisoning), whereas at thicker films (LB4), the catalyst surface was only partially poisoned leading to the appearance of two oxidation peaks in the positive potential scan, similar to those with dropcast thick films of the same particles. Importantly, the current density for formic acid oxidation was found to be markedly larger than that with dropcast films of comparable particle layer thickness, signifying the critical role of particle surface accessibility and/or ordering in the electrocatalytic performance.

Consistent results were also observed in the impedance studies, where negative impedance in the Nyquist plots and the abrupt change of sign of the phase angle in the Bode plots were seen with all three particle layers, suggesting the oxidation of surface-adsorbed CO species and the appearance of an inductive electrode. Yet the charge-transfer resistance for formic acid electro-oxidation was found to decrease with increasing film thickness, though was all smaller than that observed with dropcast thick films of the same particles. These results suggest

LB Thin Films of Fe$_{20}$Pt$_{80}$ Nanoparticles

J. Phys. Chem. C, Vol. 111, No. 36, 2007 **13459**

that there exists a minimal and optimal loading of the electro-catalysts in the electro-oxidation of formic acid, where the ordering and loading of the electrocatalysts on the electrode surface might also play an important role.

Supporting Information Available: Representative TEM micrograph of the Fe$_{20}$Pt$_{80}$ nanoparticles, AFM images of the nanoparticle dropcast films, and additional cyclic voltammo-grams of the electrodes functionalized with the particle dropcast films. This material is available free of charge via the Internet at http://pubs.acs.org.

References and Notes

(1) Lemons, R. A. *J. Power Sources* **1990**, *29*, 251−264.

(2) Steele, B. C. H.; Heinzel, A. *Nature* **2001**, *414*, 345−352.

(3) Lewera, A.; Zhou, W. P.; Vericat, C.; Chung, J. H.; Haasch, R.; Wieckowski, A.; Bagus, P. S. *Electrochim. Acta* **2006**, *51*, 3950−3956.

(4) Gurau, B.; Viswanathan, R.; Liu, R. X.; Lafrenz, T. J.; Ley, K. L.; Smotkin, E. S.; Reddington, E.; Sapienza, A.; Chan, B. C.; Mallouk, T. E.; Sarangapani, S. *J. Phys. Chem. B* **1998**, *102*, 9997−10003.

(5) Dillon, R.; Srinivasan, S.; Arico, A. S.; Antonucci, V. *J. Power Sources* **2004**, *127*, 112−126.

(6) Tian, N.; Zhou, Z.-Y.; Sun, S.-G.; Ding, Y.; Wang, Z. L. *Science* **2007**, *316*, 732−735.

(7) Frelink, T.; Visscher, W.; vanVeen, J. A. R. *Langmuir* **1996**, *12*, 3702−3708.

(8) Iwasita, T.; Hoster, H.; John-Anacker, A.; Lin, W. F.; Vielstich, W. *Langmuir* **2000**, *16*, 522−529.

(9) Motoo, S.; Watanabe, M. *J. Electroanal. Chem.* **1976**, *69*, 429−431.

(10) Jayashree, R. S.; Spendelow, J. S.; Yeom, J.; Rastogi, C.; Shannon, M. A.; Kenis, P. J. A. *Electrochim. Acta* **2005**, *50*, 4674−4682.

(11) Yang, H.; Alonso-Vante, N.; Leger, J. M.; Lamy, C. *J. Phys. Chem. B* **2004**, *108*, 1938−1947.

(12) Baldauf, M.; Kolb, D. M. *J. Phys. Chem.* **1996**, *100*, 11375−11381.

(13) Page, T.; Johnson, R.; Hormes, J.; Noding, S.; Rambabu, B. *J. Electroanal. Chem.* **2000**, *485*, 34−41.

(14) Park, K. W.; Choi, J. H.; Kwon, B. K.; Lee, S. A.; Sung, Y. E.; Ha, H. Y.; Hong, S. A.; Kim, H.; Wieckowski, A. *J. Phys. Chem. B* **2002**, *106*, 1869−1877.

(15) Lin, W. F.; Zei, M. S.; Eiswirth, M.; Ertl, G.; Iwasita, T.; Vielstich, W. *J. Phys. Chem. B* **1999**, *103*, 6968−6977.

(16) Gasteiger, H. A.; Markovic, N.; Ross, P. N.; Cairns, E. J. *J. Electrochem. Soc.* **1994**, *141*, 1795−1803.

(17) Dinh, H. N.; Ren, X. M.; Garzon, F. H.; Zelenay, P.; Gottesfeld, S. *J. Electroanal. Chem.* **2000**, *491*, 222−233.

(18) Oetjen, H. F.; Schmidt, V. M.; Stimming, U.; Trila, F. *J. Electrochem. Soc.* **1996**, *143*, 3838−3842.

(19) Goodenough, J. B.; Hamnett, A.; Kennedy, B. J.; Manoharan, R.; Weeks, S. A. *J. Electroanal. Chem.* **1988**, *240*, 133−145.

(20) Iwasita, T.; Xia, X. H.; Herrero, E.; Liess, H. D. *Langmuir* **1996**, *12*, 4260−4265.

(21) Park, S.; Xie, Y.; Weaver, M. J. *Langmuir* **2002**, *18*, 5792−5798.

(22) Lai, L. B.; Chen, D. H.; Huang, T. C. *J. Mater. Chem.* **2001**, *11*, 1491−1494.

(23) Kuk, S. T.; Wieckowski, A. *J. Power Sources* **2005**, *141*, 1−7.

(24) Gloaguen, F.; Leger, J. M.; Lamy, C. *J. Appl. Electrochem.* **1997**, *27*, 1052−1060.

(25) Chen, W.; Kim, J.; Sun, S. H.; Chen, S. W. *Phys. Chem. Chem. Phys.* **2006**, *8*, 2779−2786.

(26) Lamy, C.; Lima, A.; LeRhun, V.; Delime, F.; Coutanceau, C.; Leger, J. M. *J. Power Sources* **2002**, *105*, 283−296.

(27) Greene, I. A.; Wu, F. X.; Zhang, J. Z.; Chen, S. W. *J. Phys. Chem. B* **2003**, *107*, 5733−5739.

(28) Chen, S. W. *Anal. Chim. Acta* **2003**, *496*, 29−37.

(29) Pradhan, S.; Chen, S. W.; Wang, S. Z.; Zou, J.; Kauzlarich, S. M.; Louie, A. Y. *Langmuir* **2006**, *22*, 787−793.

(30) Templeton, A. C.; Wuelfing, M. P.; Murray, R. W. *Acc. Chem. Res.* **2000**, *33*, 27−36.

(31) Watanabe, M.; Zhu, Y. M.; Uchida, H. *J. Phys. Chem. B* **2000**, *104*, 1762−1768.

(32) Toda, T.; Igarashi, H.; Uchida, H.; Watanabe, M. *J. Electrochem. Soc.* **1999**, *146*, 3750−3756.

(33) Xia, X. H.; Iwasita, T. *J. Electrochem. Soc.* **1993**, *140*, 2559−2565.

(34) Markovic, N. M.; Ross, P. N. *Surf. Sci. Rep.* **2002**, *45*, 121−229.

(35) Rice, C.; Ha, S.; Masel, R. I.; Wieckowski, A. *J. Power Sources* **2003**, *115*, 229−235.

(36) Shiroishi, H.; Ayato, Y.; Kunimatsu, K.; Okada, T. *J. Electroanal. Chem.* **2005**, *581*, 132−138.

(37) Waszczuk, P.; Barnard, T. M.; Rice, C.; Masel, R. I.; Wieckowski, A. *Electrochem. Commun.* **2002**, *4*, 599−603.

(38) Liu, Z. F.; Ada, E. T.; Shamsuzzoha, M.; Thompson, G. B.; Nikles, D. E. *Chem. Mater.* **2006**, *18*, 4946−4951.

(39) Shao, Z. G.; Zhu, F. Y.; Lin, W. F.; Christensen, P. A.; Zhang, H. M. *J. Power Sources* **2006**, *161*, 813−819.

(40) Selvaraj, V.; Alagar, M.; Hamerton, I. *J. Power Sources* **2006**, *160*, 940−948.

(41) Kwong, C. Y.; Choy, W. C. H.; Djurisic, A. B.; Chui, P. C.; Cheng, K. W.; Chan, W. K. *Nanotechnology* **2004**, *15*, 1156−1161.

(42) Zhang, L. J.; Wang, Z. Y.; Xia, D. G. *J. Alloys Compd.* **2006**, *426*, 268−271.

(43) Tripkovic, A. V.; Popovic, K. D.; Stevanovic, R. M.; Socha, R.; Kowal, A. *Electrochem. Commun.* **2006**, *8*, 1492−1498.

(44) Aberdam, D.; Durand, R.; Faure, R.; Gloaguen, F.; Hazemann, J. L.; Herrero, E.; Kabbabi, A.; Ulrich, O. *J. Electroanal. Chem.* **1995**, *398*, 43−47.

(45) Liu, Y. C.; Qiu, X. P.; Zhu, W. T.; Wu, G. S. *J. Power Sources* **2003**, *114*, 10−14.

(46) Sugimoto, W.; Aoyama, K.; Kawaguchi, T.; Murakami, Y.; Takasu, Y. *J. Electroanal. Chem.* **2005**, *576*, 215−221.

(47) Hsing, I. M.; Wang, X.; Leng, Y. J. *J. Electrochem. Soc.* **2002**, *149*, A615−A621.

(48) Chen, A. C.; La Russa, D. J.; Miller, B. *Langmuir* **2004**, *20*, 9695−9702.

(49) Markovich, G.; Collier, C. P.; Heath, J. R. *Phys. Rev. Lett.* **1998**, *80*, 3807−3810.